High throughput quantitative tracking of *Plasmodium falciparum* clonal blood stage parasite growth and applications for antimalarial drug discovery

Zhe Cheng[*1,2], Liyang Ru[5], Andrew Hoang[2], Mingyu Wang[4], Suryanarayana Ganjikunta[2], Steven P. Maher[1], Dennis E. Kyle[*1,2,3]

[1] Center for Tropical and Emerging Global Diseases, University of Georgia, Athens, GA, USA

[2] Department of Cellular Biology, University of Georgia, Athens, GA, USA

[3] Department of Infectious Diseases, University of Georgia, Athens, GA, USA

[4] Institute of Bioinformatics, University of Georgia, Athens, GA, USA

[5] Department of Electrical and Computer Engineering, University of Florida, Gainesville, FL, USA

*Corresponding authors: Dennis.Kyle@uga.edu and Zhe.Cheng@uga.edu

Abstract

New systematic profiling of drug effects is in demand due to limitations in existing approaches to evaluate comprehensive drug effects and distinguish heterogeneity in mixed populations. One challenge is the underdeveloped methods for investigation of causal association between artemisinin induced dormancy and recrudescence in *Plasmodium falciparum*. We developed Quantitative Tracking After Chemotherapy Exposure (qTRACE) and an artificial intelligence (AI) mode to evaluate cytotoxic and cytostatic effects simultaneously at single parasite resolution in a high throughput platform. qTRACE is based upon the observation that individual parasites grow into colonies that can be quantified for numbers of viability and growth rate. Applying qTRACE, we revealed parasite-drug killing dynamics after artemisinin exposure, finding up to 50% of viable parasites arise directly from recovery of artemisinin induced dormancy. We further developed next generation qTRACE integrated with deep learning-based segmentation and analysis, thereby directly linking continuous, time-lapse phenotypes of label-free live *P. falciparum*. Our results confirmed the viability of dormant ring stages and that recovery rates differ between artemisinin-susceptible and -resistant *P. falciparum*.

47 **Main**

48 Accurate evaluation of drug induced effects and parasite viability is essential for
49 discovering new anti-malarial drugs and monitoring the success of currently used regimens.
50 Previously, evaluation of susceptibility to anti-malarial drugs is measured by half-maximal
51 inhibitory concentration (IC50) or various ring stage survival assays[1-5]. These assays are carried
52 out in a bulk culture for short periods of time, after which susceptibility of drugs is measured by
53 comparing the number of replicated parasites between treated and untreated condition. Many of
54 these methods rely on taking aliquots from a large culture and only capture a single snapshot.
55 Drug perturbation assessments often lack insights into drug effects and are unable to
56 differentiate growth inhibition and temporary arrest with killing. More critical limitations include
57 the inability to evaluate long-term drug-parasite dynamics as the measurements are not derived
58 from the same individual cells and cannot resolve heterogeneity in a mixed population. Too
59 often the result is a misinterpretation of killing rate or that no viable parasites remain in the
60 short-term assay. Conversely, previously published data suggest persistent survivors exist and
61 that standard assays obscure true killing effects of drugs and hinder the development of next
62 generation anti-malarial drugs[6]. Consequently, these methods create inconsistent correlations
63 between drug susceptibility and genotypes, while ignoring valuable biological insights of
64 individual diversity of parasites and drug effects in a continuous system.

65 Artemisinin combination therapy is the frontline treatment for *P. falciparum* infection.
66 However, the emergence and spread of resistance to artemisinin poses a significant threat in
67 malaria control[7]. Delayed clearance and recrudescence are frequently associated with
68 artemisinin resistance clinically[8]. It has been widely reported that exposure to artemisinin drugs
69 induces a phenotype known as artemisinin-induced dormancy and these dormant parasites can
70 persist for many days before they either recover or die. Numerous studies suggest these
71 dormant parasites play a role in infection recrudescence and treatment failures both clinically

72 and in vitro[9-13]. Drug-induced cell cycle arrest has been widely observed in many human
73 diseases, including malaria, and have posed a significant challenge in searching for improved
74 therapies[6]. Thus, understanding the role of dormancy with artemisinin resistance and parasite
75 recrudescence is critical for formulating effective counterstrategies. However, the causal relation
76 of artemisinin induced dormancy to parasite survival and recrudescence remains poorly
77 understood due to limitations in existing approaches. Some of the various assays attempt to
78 compensate for delayed recovery and quantify dormancy recovery, but still face the same flaw
79 that early survivors can easily disguise the existence of parasites that recover later in a mixed
80 culture[2, 14]. An improved and more efficient evaluation of artemisinin effects and quantification of
81 artemisinin induced dormancy are needed to accurately quantify drug resistance at the clonal
82 level.

83 In this study, we developed Quantitative Tracking After Chemotherapy Exposure
84 (qTRACE) to quantify viability and growth at single parasite resolution based on the concept that
85 following an adequate dilution of parasitized erythrocytes, one parasite grows into a colony that
86 can be visualized microscopically. qTRACE is a versatile method that simultaneously tracks
87 survival, time-dependent recovery, and drug-induced growth effects. We demonstrated the
88 robustness of qTRACE by revealing true long-term drug effects of dihydroartemisinin (DHA) on
89 multiple *P. falciparum* isolates and cloned parasites with diverse backgrounds. We further clarify
90 the underappreciated contribution of artemisinin induced dormancy in parasite recrudescence
91 and reveal the undiscovered growth retardation effect of artemisinin drugs in selected parasite
92 strains. Further development of qTRACE AI with deep learning-based cellular analysis
93 effectively enhanced time-lapse biological connection, generalization, and accuracy through
94 unrestricted observation of label-free live cell phenotypes. Applying qTRACE to drug screening,
95 we found a diverse cytostatic and cytotoxic effect preference and time-dependent dynamics
96 between drugs and parasites. qTRACE is strongly positioned for holistic investigation into single

97 cell level drug-parasite dynamics while remaining amendable to high-throughput and logistically
98 complex time course experiments.

99 **Results**

100 **Quantification of longitudinal viability and growth of single parasites**

101 We found that, when sufficiently diluted in a 384 well microtiter plate, one single parasite
102 grows into a colony and can be continuously monitored over time. These initial observations led
103 us to develop a high throughput and high content imaging assay. A previously developed GFP
104 integrated parasite (NF54-GFP) was seeded into 384 well microtiter plates and imaged
105 continuously using a 4x objective on a high content imaging system (HCI)[15]. In these assays, we
106 observed continuous formation and growth of colonies over 22 days (Fig. 1A). Day 5 was the
107 earliest time we could detect a colony, likely due to insufficient fluorescence intensity at low
108 magnification at earlier time points. Due to the care taken to not disturb the plates during the
109 time course, these colonies continued to grow at the same position in the well throughout the
110 duration of the assay (22 days) (Fig. 1A). Meanwhile, we also observed parasite recovery and
111 colony growth in ring stage *P. falciparum* exposed to 700nM DHA for 6h (Fig. 1A). Notably, some
112 colonies appeared early, with others at later timepoints, which is consistent with the concept that
113 artemisinin drugs induce ring stage dormancy, followed by delayed recovery of the parasites
114 (Fig. 1A). Time-lapse imaging showed the differential onset of growth of individual parasites,
115 with late recovering parasite colonies from dormancy detected in the same well alongside early
116 recovering parasites (Supplementary Video 1). Comparison of GFP, Hoechst, and DIC imaging
117 showed complete overlap of the identified colonies which confirms these colonies consist of
118 parasites (Fig. 1B). We chose to use Hoechst-staining of DNA as the fluorescent marker as this
119 route enables assessment of clinical isolates without integrated fluorescent markers. At
120 increased magnification (60X and 100X), we show that a colony consists of hundreds-to-
121 thousands of parasites, evidenced by imaging of individual parasites and foci of hemozoin (Fig.

122 1C). The growth of parasites results in reduced hemoglobin that appears as an opaque clearing
123 in the red blood cell monolayer, consistent with previous study of plaque forming in *P.*
124 *falciparum*[16] (Fig. S1A). A z-stacked video of a colony imaged with a 100X objective shows that
125 parasites are distributed horizontally and vertically throughout the packed red blood cell layer
126 (Fig. S1B and Supplementary Video 2).

127 These phenotypes, therefore, can be used to quantify the growth of individual parasites
128 (Fig. 1D and S1C). Long-term measurements at multiple time points allow for longitudinal
129 measurements of parasite growth and identification of slow growing or late recovering parasites
130 (Fig. S2). To validate the single parasite-to-colony concept and quantification reliability, we
131 performed a serial dilution experiment to assess correlation between colony number and
132 parasite input (Fig. S3A). Measurements of total DNA content showed a successful serial
133 dilution of parasites (Fig. S3B). From the same experiment, quantification of colonies from wells
134 seeded with $\leq$2500 cells correlated with the total DNA content of parasites; however, the first
135 two dilution points resulted in overlapping colonies which lead to inaccurate quantification (Fig.
136 1E). In wells with lower numbers of parasites, the average quantified colonies in each well were
137 within one dilution of the expected number of colonies (Fig. 1F). Taken together, these results
138 demonstrate that one colony comes from replication of one single parasite and quantification of
139 colonies can be used to track the original number of viable parasites in each well.

140 **qTRACE tracks single parasite survival, time-dependent recovery and growth**

141 Initially, we developed qTRACE to improve our understanding of survival and recovery
142 from artemisinin exposure and artemisinin-induced ring stage dormancy phenotypes (Fig. 2A).
143 To ensure sufficient identification of late recovery of dormant parasites, we designed the assay
144 to last 22 days in duration, with multiple plates prepared for multiple timepoints throughout (Fig.
145 2A). To minimize liquid movement in the blood layer and to preserve colony integrity, we
146 designed a robotic automation protocol to perform slow liquid manipulation with essentially no

147 disruption to the blood layer (Figure S4A). At every timepoint, one plate was fixed and stained
148 for HCI while the remaining plates underwent media change using the designed no-disruption
149 protocol (Fig. 2A).

150 We developed a single-parasite viability index (SVI) to compute the viability from drug
151 treatment based on quantification of colonies. We can determine the viability of single parasites
152 at time t for strain s:

153 $$SVI\ (s,t) = \frac{\text{Treated colony counts (s,t)}}{\text{D(s) x Untreated colony counts (s,t)}} \text{x}100$$

154 SVI is the ratio of the number of colonies between treated and untreated conditions
155 normalized to single parasite division. D(s) is the determined dilution factor between treated
156 sample and untreated sample for strain s. The introduction of factor D enables greater tolerance
157 of experimental variability caused by cell density (Fig. S4B). Additionally, the factor D can be
158 adjusted to compensate for different levels of drug sensitivity of different genotypes. SVI showed
159 minimal variation under different D factors because the overall percentage of viability remained
160 unchanged (Fig. S4C).

161 The length of qTRACE experiments is flexible and a single timepoint qTRACE SVI
162 assessment is sufficient for evaluating drug killing and parasite survival, which requires no
163 media change and can be applied with manual manipulation (e.g., multi-channel pipettes) (Fig.
164 2B). In this study, we used day 7 as the timepoint to assess initial survival from artemisinin
165 exposure. By adding time points to generate time-dependent SVI, we observed cumulative
166 recovery overtime at single parasite resolution (Fig. 2C). This made it possible to identify and
167 quantify parasites that recovered late. In addition to evaluation of multiple parasite strains
168 treated with a single inhibitor, qTRACE also is compatible with high-throughput drug screening
169 (Fig. 2A). In a dose response experiment, we assessed drug killing effects at different
170 concentrations (Fig. 2D).

171 Through quantification of the colony size over time, we captured the exponential growth
172 of viable parasites (Fig. 2E). These data are useful to evaluate effects of drug on parasite
173 growth, making cytostatic effects measurements a convenient secondary outcome from
174 qTRACE. Moreover, quantification of the area of colonies alongside viability enables
175 identification of late recovered dormant parasites and assessment of growth behavior of those
176 recovered parasites. To quantitatively determine growth difference between two samples, we
177 adapted the growth rate inhibition metrics (GR) from a previous study[17]:

178 $GR = 2^{k(T)/k(U)}-1$

179 In our application, k(T) is the growth rate of drug-treated parasites and k(U) is the growth
180 rate of untreated controls. Similarly, the GR value can also be used to quantitatively assess
181 fitness difference between strains, where k(T) was the growth rate of strain 1 and k(U) was the
182 growth rate of strain 2. The GR value ranges from -1 to 1, with 1 suggesting no impact on
183 growth, 0 meaning complete growth inhibition and negative value indicating cytotoxic effects.
184 Using GR and SVI together we differentiated between cytotoxic and cytostatic effects of a drug.

185 **qTRACE reveals time-dependent viability of single parasites after DHA exposure and**
186 **diverse mechanisms of artemisinin induced dormancy**

187 Mutations in the *P. falciparum* K13 propeller domain are known to facilitate resistance to
188 artemisinin drugs[18]. To study how K13 mutations affect the viability of parasites, we compared
189 Dd2 with its K13 mutants Dd2-K13-C580Y and Dd2-K13-R539T using qTRACE[19]. Rings at 0-
190 3hpi were exposed to 700nM DNA for 6 hours before plating (Fig. 2A). As expected, we
191 captured the number and the size of growing colonies from all three strains and observed
192 significantly fewer colonies from DHA treated Dd2 compared to its isogenic K13 mutants (Fig.
193 3A). Overall, both DHA treated and untreated colonies kept growing throughout the assay
194 duration (Fig. S5A). Interestingly, a wide distribution of colony sizes was observed even in

195 synchronized untreated controls, presumably due to genuine growth variability as previously
196 noted[20] (Fig. S5A). qTRACE single timepoint assessment of SVI on day 7 revealed differences
197 in susceptibility to DHA among three strains (Fig. 3B). All three strains continued to show
198 increased viable parasites over time until reaching a plateau, indicating that the initial survivors
199 only represent a fraction of the total parasites that eventually recover following exposure to DHA
200 (Fig. 3C). These results demonstrate that both Dd2 and its K13 mutants exhibit dormancy
201 phenotype for survival and that mutated K13 facilitated resistance is manifested on both initial
202 survivors and recovery from dormancy mechanisms. Dd2-K13-R539T exhibited over 100-fold
203 more viable parasites after exposure to DHA, whereas Dd2-K13-C580Y showed a
204 comparatively lower difference compared to the parental Dd2 (Fig. 3D). This is consistent with
205 previous reports showing that the R539T mutation confers a higher level of resistance than
206 C580Y[18, 21]. The fold change remained stable for all three strains, indicating that although higher
207 number of parasites recovered in K13 mutans, the proportion of late recovery remained similar
208 across three strains.

209 To investigate if the delayed recovery from DHA is a common strategy of survival, we
210 tested various other laboratory-adapted *P. falciparum* lines and clinical isolates. We tested two
211 parasite lines and their progenies that were previously selected for artemisinin resistance (D6,
212 D6R, W2 and W2R)[9]. Both W2/W2R and D6/D6R pairs showed different levels of resistance to
213 DHA exposure and continued to have parasites recover over time (Fig. S5B and S5C). The
214 decreased fold change of viability between W2 and W2R shows that W2 has more viable
215 parasites coming from delayed recovery than W2R, presumably because W2R adapted
216 stronger DHA tolerance during resistance selection (Fig. S5B). The viability difference between
217 D6 and D6R was greater than that between W2 and W2R, presumably because D6R went
218 through a longer selection period than W2R (Fig. S5C)[9]. Overall, the in vitro drug selected
219 parasites exhibited lower levels of resistance compared to parasites with mutated K13, yet

220 recovery from artemisinin-induced dormancy was observed in both genotypes (Fig. 3C, S5B
221 and S5C). We next tested NHP-4781 which has E252Q K13 mutation that is located outside β-
222 propeller domains[22]. NHP-4781 showed a comparative level of susceptibility to DHA exposure
223 compared to Dd2, indicating that mutation outside propeller domain on K13 does not incur
224 resistance to artemisinin, which is consistent with previous findings[21] (Fig. 3E and Fig. S5D).
225 TM91-C235 is a multi-drug-resistant parasite derived from patient with multiple drug treatment
226 failures[23]; it showed moderate resistance compared to D6 and Dd2, but not to W2 (Fig. 3E and
227 Fig. S5D). The ability to have more continuous dormancy recovery of W2 compared to other
228 parasite strains is consistent with previous study which showed higher and longer recovery of
229 W2 after DHA exposure (Fig. 3E)[14].

230 The nine *P. falciparum* lines tested showed different levels of delayed recovery from DHA
231 (Fig. S5E). Notably, the initial survival measured on day 7 from DHA strongly correlates with late
232 recovery, indicating that, despite the differences of susceptibility to DHA among these parasites,
233 the survival is equally exhibited by the initially survived parasites and parasites recovered from
234 dormancy (Fig. 3F). For many of the artemisinin sensitive parasite lines, delayed recovery
235 parasites accounted for about half of the total parasites that eventually survived DHA exposure
236 (Fig. 3G). A decreased proportion of late recovered parasites in both K13 mutants and in vitro
237 selected lines suggests that an increased level of resistance reduces the reliance on dormancy
238 as a mechanism to survive (Fig. 3G). The large portion of delayed recovered parasites is often
239 overlooked in many studies that use standard 72-hour assays to estimate parasite killing but
240 now can be more accessibly evaluated using qTRACE.

241 **qTRACE assesses growth inhibition and fitness**

242 Through measurements of the growing colonies, qTRACE allowed us to quantify growth
243 inhibition imposed by drugs and fitness differences between parasite lines. From the same DHA
244 exposure experiments described above, we analyzed the growth and distribution of colonies of

245 DHA treated Dd2 and its K13 mutants. We found the growth of the two K13 mutants mimics
246 their untreated control, while the growth of Dd2 was severely affected by DHA, as evidenced by
247 the dispersed distribution (Fig. 4A). Comparison of growth curve and GR value showed Dd2
248 suffered a reduced growth rate after DHA exposure, whereas K13 mutants showed overlapped
249 growth with their control (Fig. 4B and 4C). These results suggest that Dd2 K13 mutant parasites
250 can quickly adapt to normal growth once recovered from DHA, but the growth of many parental
251 Dd2 parasites become impaired by DHA. Many previous studies showed that adaptation to drug
252 resistance sometimes induces fitness costs in the parasites[10, 24]. Through qTRACE, we can
253 detect fitness disadvantage in the Dd2-K13-C580Y, but not in the Dd2-K13-R539T, compared to
254 parental Dd2; which is consistent with previous reports[21] (Fig. 4D). In the case of in vitro
255 selected lines, W2R showed a fitness disadvantage compared to W2, while D6R showed a
256 more minor disadvantage compared to D6 (Fig. S6A), as noted previously[10]. DHA exposure
257 resulted in reduced growth and lowered GR for W2 and D6, yet W2R and D6R phenocopied the
258 growth of untreated conditions (Fig. S6B and S6C). C235 showed a slight impact on growth rate
259 from DHA exposure (Fig. S6D). NHP-4781 also exhibited retarded growth following DHA
260 exposure, as well as poor adaptation to culture as seen by the slow growth in the untreated
261 control (Fig. S6E). This is supported by the observed gametocyte formation even during routine
262 culture. Total viability from artemisinin exposure showed a moderate correlation with GR,
263 indicating that increased resistance to artemisinin led to decreasing growth impact on the viable
264 parasites, but was also parasite background dependent (Fig. 4E). Together, these results
265 demonstrate that resistance to artemisinin is also reflected in the ability to quickly resume
266 growth upon recovery.

267 **Application of qTRACE in drug testing**

268 The ability to assess phenotypes of single parasites is a valuable tool to improve
269 accuracy of drug susceptibility testing (Fig. 2A). We applied qTRACE to drug screening and

270 tested 15 common anti-malarial drugs on Dd2 parasites (Fig. S7A and Supplementary Table 3).
271 Consistent with previous reports of Dd2 background, qTRACE also demonstrated elevated
272 resistance to sulfadoxine and pyrimethamine in Dd2[25]. The SVI50 of most compounds tested
273 showed comparable results to the standard IC50 measurements in a bulk culture, indicating
274 strong reproducibility of qTRACE to serve as a quantitative alternative to conventional bulk
275 methods (Fig. S7B and Supplementary Table 3). qTRACE also demonstrated extraordinary
276 efficiency and improvements of throughput due to very low parasite input requirements (less
277 than 50 parasites per well).

278 **qTRACE AI powered by deep learning enables continuous label-free live cell analysis**

279 From the development of qTRACE with DNA dyes, we noted one of the major limitations
280 is the lack of continuity between every timepoint in a continuous experiment when not using
281 self-reporting parasite isolates (e.g., GFP) (Fig. 2A). To enable continuous observation of the
282 same samples and preserve clone identities, we incorporated a deep learning-based semantic
283 segmentation method into qTRACE. The next generation qTRACE AI directly quantified objects
284 on images acquired through transmitted light microscopy without the need to fix, stain, or
285 genetically modify the parasites. A total of 5760 distribution-calibrated images spanning diverse
286 experimental applications were used to train convolutional neural networks (CNN) (Fig. 5A).
287 These images covered different time points and sizes of colonies, but with a stronger focus on
288 early times to compensate for increased difficulty of learning to differentiate small colonies (Fig.
289 5B and S8A). Parasite colonies of every transmitted light image were annotated to polygons by
290 trained human professionals using ground truth GFP images as reference (Fig. 5C).

291 We trained on CNN model U-Net architecture because of its established capability of
292 biomedical level semantic segmentation (Fig. 5D and S8B). Overall, qTRACE AI achieved
293 comparable human level accuracy, demonstrated by the strong correlation between annotated
294 results and model predicted results (Fig. 5E). Mean absolute error (MAE) of count quantification

295 showed an average of 2.63 and is relatively stable over time, while area pixel error increased
296 slightly in later timepoints (Fig. 5F and Supplementary Table 4). Most of the test images showed
297 identical quantification between annotated results and predicted results across various
298 conditions (Fig. S9A). However, the true accuracy of qTRACE AI is underestimated here
299 because we noticed most of the disparities between annotated results and predicted results
300 were due to human errors in annotations. In almost all instances, our trained CNN model was
301 able to correct human errors, including filtering debris and false positives, and to identify true
302 positive colonies that were originally omitted by human observations (Fig. S9B and S9C).
303 Additionally, the label-free image analysis of qTRACE AI removed the most common challenge
304 of dealing with fluorescent noise during imaging as we routinely saw images that would have
305 been unsuitable for analysis due to high fluorescent background (Fig. S9D). Since qTRACE AI
306 does not have any benchmarking available, we decided to train a second model using Vision
307 Transformers (ViT) to allow for a performance comparison (Supplementary Table 4). Overall, U-
308 Net architecture showed superior performance compared to ViT for both count and area
309 quantification tasks (Supplementary Table 4). The performance differences between
310 architectures may be attributed to the data-efficiency characteristics of each model. Thus far, the
311 capability of qTRACE AI to track live single parasites greatly enhances accuracy and flexibility
312 over DNA stain qTRACE protocol, making it more suitable for diverse applications, including
313 demanding long-term studies that may yield new insights into drug effects (Fig. 5G).

314 **qTRACE reveals new insights into drug activities and effects**

315 We screened a Medicines for Malaria Venture (MMV) antimalarial reference library to
316 derive both SVI50 and GR50 using qTRACE AI label-free imaging analysis (Fig. 6A). A
317 correlation study of qTRACE AI and qTRACE side by side showed excellent reproducibility
318 between the two methods for viability and growth assessments (Fig. 6B). Most of the tested
319 drugs showed similar dose response curves between qTRACE AI and qTRACE (Fig. S10A).

320 These results confirmed the feasibility of qTRACE AI to obtain validated results from more
321 typical experimental applications. Through the evaluation of SVI50 and GR50, we identified
322 diverse drug induced cytotoxic and cytostatic effects from tested compounds. (Fig. 6C and
323 Supplementary Data 1). Azithromycin showed strong growth inhibition evidenced by the much
324 lower GR50 and the inhibition of growth at lower concentration as seen in the GR curve, while
325 pantothenamide showed clear cytotoxic effect (Fig. 6C and S10B). Understanding time-
326 dependent drug effects is crucial for dosing and pharmacokinetic studies. To take advantage of
327 the unlimited continuous live cell imaging of qTRACE AI, we performed a time-lapse experiment
328 to assess the time-dependent potency of compounds from the same cells over time. We
329 observed all three types of time-dependent activities, either increasing, decreasing or stable
330 over time (Fig. 6D). We detected 23 drugs that gradually lost potency, while only 3 drugs gained
331 extra potency with at least 2-fold change over time (Fig. 6D and Supplementary Data 1).
332 Azithromycin showed the greatest potency increase in the library, as well as mirincamycin,
333 another known slow acting drug[26, 27] (Fig. 6E). KAE609, KAF156 and some other drugs showed
334 strong stability over time, while many of the drugs lose their effect over time (Fig. 6E and
335 Supplementary Data 1). From these results, we conclude that qTRACE is capable of being used
336 as a significant enhancement over conventional drug testing to reveal more insightful drug
337 effects at single parasite resolution.

338 **Discussion**

339 The development of qTRACE was originally driven by the ambition to elucidate the
340 confounders in artemisinin induced dormancy and to quantify viable parasites that result in
341 recrudescence. Numerous studies have suggested the association between artemisinin
342 resistance and artemisinin induced dormancy, yet there have been limitations in quantifying
343 viable parasites that recover later than the first recrudescent brood[9, 10, 12, 14, 28]. qTRACE
344 overcomes those limitations by tracking the viability and growth of individual parasites, thereby

345 effectively distinguishing initial survivors and late recovered parasites in an automated high
346 throughput manner. Our results confirmed that recovery from artemisinin-induced dormancy
347 plays a significant role in overall parasite survival at the population level, with nearly half of the
348 viable parasites arising from dormancy recovery. Given that day 7 was the first point of
349 measurement, the proportion of delayed recovery is likely underestimated. In this study, we
350 show that the ability to survive artemisinin drugs in K13 mutants are not only exhibited by the
351 large number of initial survivals, but also in the delayed recovery from dormancy (Fig. 3C, 3F
352 and 3G). In fact, the number of parasites recovered from dormancy could be underestimated
353 due to limited space in the well for higher resistant lines (both Dd2 K13 mutants) in later
354 timepoints (Fig. 3C). The ability to utilize dormancy as a survival mechanism in both sensitive
355 and resistant parasites suggest dormancy is an innate survival mechanism and likely
356 independent of genomic resistance mechanisms. Resistance mechanisms improve initial
357 adaptation and stress response to artemisinin drugs through each of their pathways, allowing
358 more parasites to survive as well as more parasites to utilize dormancy. On the other hand,
359 more sensitive parasites have overall lower initial survival and lower dormancy recovery rates
360 due to poor initial response to artemisinin. Previous study suggests that dormant parasites are
361 resilient to a wide spectrum of anti-malarial drugs, indicating the reduced efficacy of ACT partner
362 drugs to remove dormant parasites[12]. Given the large portion of late recovery after DHA
363 exposure, it would be reasonable to attribute the clinically observed recrudescence to the
364 recovery of dormant parasites. In fact, parasites going into dormancy may be a favored survival
365 path during ACT treatment because of the reduced susceptibility to drugs and the half-lives of
366 the partner drug.

367 Investigation of cytostatic drug effects and fitness costs associated with increased
368 resistance constitute a large study domain in drug discovery and drug resistance. The cytostatic
369 effects of many anti-malarial drugs remain poorly studied due to lack of approaches to properly

370 evaluate them in a large scale. Our ability to track individual parasites with qTRACE made it
371 possible to evaluate cytostatic effects in a high throughput and technically straightforward
372 manner. Across nine parasite lines, we observed varying cytostatic effects induced by
373 artemisinin, influenced by genetic backgrounds and a moderate correlation of decreased growth
374 inhibition to increased resistance.

375 Altogether, our results demonstrate that resistance to artemisinin is a multifaceted
376 phenotype. When resistance increases, the proportion of initial survival and recovery from
377 dormancy equally increases, meanwhile the impact on growth gradually decreases until there is
378 no more growth impact, but in a parasite background dependent manner. The dormancy effects
379 of artemisinin drugs cannot be underestimated and is likely the ultimate culprit behind frequently
380 reported recrudescence. It is imperative that future ACT development and artemisinin resistance
381 studies incorporate dormancy recovery as a standard evaluation.

382 Previous studies on fitness typically include laborious processes and error prone
383 techniques, such as large amount of microscopy counting or combining two different parasites
384 into one culture[10, 24, 29]. In this study, we showed that fitness assessment is a convenient
385 secondary outcome when conducting qTRACE for other purposes, such as testing inhibitor
386 effects. With the emergence of qTRACE, fitness studies will no longer need to be a complicated
387 independent experiment. The growth assessment capability of qTRACE will be useful to a wide
388 range of research, including but not limited to evaluating growth competition and growth
389 inhibition, such as one imposed by RNAi or nutrition starvation.

390 Integration of deep learning-based analysis into qTRACE AI effectively overcame the
391 limitation of having disconnected results at every timepoint. The U-Net architecture CNN model
392 is well suited for qTRACE, evidenced by strong learning of the pattern with limited datasets. We
393 found that qTRACE AI is superior to DNA stain qTRACE for its excellent generalization,
394 accuracy, and cellular information linkage. qTRACE AI uses a single pipeline for all the

395 experimental conditions, while in many cases different sets of rules are needed for DNA stain
396 qTRACE depending on the timepoints or applications. Debris and background signals are
397 among the most difficult noises to remove in rule-based image analysis because most of the
398 time they fall into similar characteristic regions to the true objects. qTRACE AI demonstrated
399 strong ability to handle those difficult situations (Fig. S9B, S9C and S9D). Lastly, label-free
400 continuous live cell observation ensured the most authentic connection of cell behavior over
401 time, and significantly improved our ability to identify unique signatures for each individual
402 parasite. qTRACE AI and original DNA stain qTRACE will serve as great complement for each
403 other to improve versatility and accessibility.

404 When applied to drug screening, qTRACE demonstrated its ability to serve as a direct
405 replacement to currently used dose response assays. SVI50 and GR50 derived from qTRACE
406 are robust alternatives to IC50 as the measurements were derived on a per parasite basis. For
407 routine drug testing, a single endpoint at 120h is sufficient to identify different effects and does
408 not require any robotic automation. Taking advantage of deep learning-based continuous label-
409 free imaging, we screened an anti-malarial drug reference library and revealed new insights into
410 both cytotoxic and cytostatic effects imposed by drugs, which will improve understanding of the
411 mode of action of a drug and its future development. Through continuous measurements,
412 qTRACE outputs time-dependent drug potency shifts, which can serve as foundation for drug
413 pharmacodynamics and drug combination studies. Equally important to accurate drug effect
414 evaluation is improved efficiency; qTRACE increases drug screening throughput by up to 667-
415 fold. Typical dose response assay uses >1% parasitemia culture (~2000 parasites/μl in 2%
416 hematocrit), while qTRACE only needs less than 3 parasites/μl.

417 qTRACE is based on the biological phenomenon that a single parasite grows into a
418 colony. The concept of colonies and plaque assays have been widely used in various biological
419 research. In malaria research, similar concepts have been previously proposed, yet there has

been little application and requires visual inspection of plaques[16]. Integrated with HCI, automation and deep learning, we developed a versatile application of this biological phenomenon and removed many of the previously suggested limitations, such as long waiting time and hematocrit limits. The flexibility to change media and supplement fresh blood is crucial for any long duration experiments. Here we have demonstrated that currently available compact automation stations are sufficient to achieve media change without disrupting colony integration, though it is not required for many of the applications shown in the report. Potential applications of this concept are far beyond what has been demonstrated in this study. Because of the ability to identify the number of colonies in each well, it becomes possible to map genomic and transcriptomic signatures associated with differential conditions at monoclonal levels. More advanced utilization could improve the selection of drug resistance by picking parasites that recover early or recover late, depending on if the purpose was to select for initial survivors or study latency mechanism(s).

In summary, qTRACE will serve as an all-around method that can be used for a wide range of scenarios, effectively overcoming previous limitations to achieve single parasite level insights. It would be appropriate to use qTRACE as a routine assessment of the recrudescence risks of developing compounds and current treatment combinations.

443 **Methods**

444 **Parasite culture**

445 The parasites used in this study include Dd2, Dd2-K13-C580Y and Dd2-K13-R539T (genetically
446 modified Dd2 strains containing mutation on K13 PF3D7_1343700); D6 and D6R (an in vitro
447 selected artemisinin resistant progeny of D6); W2 and W2R (an in vitro selected artemisinin
448 resistant progeny of W2); C235; NHP-4781; and a genetically modified NF54-GFP (inserted
449 GFP in cg6 locus)[9, 15, 19, 23]. For routine culture, parasites were grown at 37°C at 2% hematocrit
450 in RPMI 1640 media (Gibco) supplemented with 25mM HEPES and 24mM $NaHCO_3$, and with
451 10% heat-inactivated human A+ plasma and 10 µg/ml gentamycin. Cultures were maintained in
452 a gas chamber with 5% O_2, 5% CO_2, and 90% N_2. Giemsa slides were routinely made to assess
453 parasite growth and stages. The growth media was changed every two days, and fresh blood
454 was added when needed. Cultures were tested and found negative for mycoplasma regularly
455 during this study.

456 **Ring Stage 0-3hpi Synchronization**

457 The same 2-step synchronization protocol was performed to achieve 0-3h post invasion (hpi) for
458 all strains used in this study. First, late stages were selected by laying on top of 65% percoll
459 gradient and followed by centrifugation at 1500RCF[30]. Three hours later, freshly invaded rings
460 were selected using 5% D-sorbitol [31]. After each synchronization step, parasites were washed
461 with RPMI 1640 media. Synchronized 0-3hpi parasites were allowed to reinvade before being
462 used for experiments.

463 **Dihydroartemisinin (DHA) exposure**

464 The same DHA treatment was used for all DHA exposure experiments in this study. Tightly
465 synchronized 0-3hpi parasites were adjusted to 1% parasitemia and 2% hematocrit and treated

466 with 700nM DHA. Six hours later, DHA was removed by centrifugation and washing with RPMI
467 1640 media before being replaced with culture media.

468 **GFP live cell time lapse imaging and fluorescent imaging**

469 For GFP continuous imaging, 0-3hpi NF54-GFP parasites were seeded into 384 well plates
470 (Greiner Bio-one) with an estimated number of 10 parasites per well. The same plate was taken
471 for imaging on day 3, 5, 7, 10, 13, 16, 19, 22 using Lionheart (Agilent). Media was changed at
472 day 7, 10, 13, 16, 19 by removing and replacing 20µl of media using NXP workstation
473 (Beckman). Another experiment with 6h DHA exposure was performed in a similar way except
474 the initial plated parasites were 1000 parasites per well. To image parasite using both Hoechst
475 staining of DNA and GFP expression, 40ul of 5ug/ml Hoechst was added into the plate and
476 maintained for 30 minutes before imaging. High magnification images were obtained using the
477 100x objective on a DeltaVision II (GE Healthcare) with deconvolution of a 22-plane Z-stack
478 using Software (GE healthcare).

479 **qTRACE**

480 **Metrics**

481 Colony counts and colony areas in the presence of drug are normalized to untreated controls in
482 the same plate under the same growth conditions. Technical replicates were averaged to yield
483 an average colony counts or colony area. For single candidate testing, we typically collect from
484 48-176 technical replicates. For dose response, two technical replicates per plate were
485 collected.

486 Single-parasite viability index (SVI) was calculated to evaluate the viability of parasites and the
487 cytotoxic effects of the testing drugs. SVI of parasite strain (s) at timepoint (t) was calculated as:

488 $$SVI\ (s,t) = \frac{\text{Treated colony counts (s,t)}}{\text{D(s)x Untreated colony counts (s,t)}} \text{ x } 100$$

489 The average number of colonies for each parasite strain growing at each condition at every
490 timepoint was calculated and normalized to the average number of colonies from the control.
491 (D) represents the dilution factor between treated and untreated in a multi-strain testing design.
492 SVI is a percentage value and ranges from 0 to 100, 0 meaning no viable parasite exists and
493 100 means no effect on parasite viability from the treatment condition. In recovery experiments,
494 Survival SVI is defined as the SVI form the first point of measurement. The Max SVI
495 measurement after the first timepoint is defined as the maximum possible viability or max SVI.
496 Maximum delayed recovery is calculated as Max SVI – Survival SVI. When calculating SVI for a
497 range of concentrations, SVI50 is the concentration that confers half maximal drug effect on
498 parasite viability.

499 Growth rate inhibition (GR) was adapted from a previous study to evaluate the growth of every
500 viable parasite[17]. The average area of colonies for each parasite strain growing at each
501 condition at every timepoint was calculated and normalized to the average area of colonies from
502 control. GR value ranges from -1 to 1, with 1 meaning no impact on growth, 0 meaning
503 complete growth inhibition, and -1 meaning highest cytotoxicity. When calculating GR for a
504 range of concentrations, GR50 is the concentration when GR = 0.5, which refers to half maximal
505 growth inhibition.

506 For continuous measurements from multiple timepoints, an exponential growth curve was fitted
507 for each parasite strain and each condition. GR was then calculated:

508 $GR = 2^{k(T)/k(U)}-1$

509 The growth rate (k) of each fitted curve was extracted, with k(T) representing the growth rate of
510 drug treated condition and k(U) representing the growth rate of untreated controls. Alternatively,
511 when testing fitness or growth competition between two strains, k(T) became the growth rate of
512 strain 1 and k(U) became the growth rate of strain 2 or reference strain.

513 When measuring qTRACE as a single timepoint experiment, GR was calculated as:

514 $$GR = 2^{\frac{log_2(x(T)/x_0)}{log_2(x(U)/x_0)}} - 1$$

515 In this equation, x(T) represents the average area in drug treated conditions and x(U) is the
516 average area in untreated control. X_0 is the starting area; this could be the measurement before
517 starting the experiment or be fitted as an estimated area of a single parasite because colonies
518 originate from single replicating parasites.

519 **Single candidate qTRACE**

520 This method was designed to test the response of multiple parasite lines to a single testing
521 candidate of interest. In this study, DHA was used as an example. Synchronized 0-3hpi
522 parasites were treated with DHA for 6h using the procedure described above. An estimated
523 number of 10-50 parasites per well were seeded for untreated control for each parasite line.
524 Depending on the designed D factor for each parasite line, D*number of parasites in untreated
525 controls for each treated samples were seeded into the same plates with the untreated controls
526 based on similar design shown in Fig. 2A. Based on different timeline design, at every timepoint,
527 one plate was taken for staining and thereafter imaging quantification; the rest of the plates
528 were taken for media change using designed no disruption protocol on NXP workstation to
529 minimize blood layer disruption.

530 **Evaluating altering condition of qTRACE**

531 Altering condition experiments were performed to characterize the tolerance of qTRACE to
532 variations. For changing seeding density, D = 100 was used and the estimated seeding parasite
533 in untreated wells ranged from 5-50. For changing D factor, an estimated 30 parasites per well
534 in untreated wells were used.

535 **Dose response qTRACE**

536 This method was designed to test the effect of compounds in a high throughput format using
537 qTRACE. Compounds were tested in a 12-point semi log dilution in duplicates. Synchronized 0-
538 3hpi parasites were seeded into 384 well plates with 50-100 parasites per well. The seeded
539 plates were then drugged with the source plate using pintool affixed to the NXP (V&P Scientific).
540 For single endpoint experiments, plates were fixed and stained at 120h. For time lapse
541 experiments, whole plates were imaged using transmitted light at 48h interval followed by
542 qTRACE AI analysis.

543 **Curve fitting**

544 For experiments containing multiple timepoint, an exponential growth curve was fitted using the
545 average colony area measured at each timepoint for each condition:

546 $Y = Y_0 * \exp\,(K * t)$

547 The fitted parameters are:

548 Y_0: the best fitted starting value when t = 0.

549 K: the growth constant of the fitted curve for the condition and parasite line used

550 t: time

551 In the case of a comparison between two fitted curves, Y_0 was restricted to untreated control or
552 the reference parasite strain. K was extracted for calculation of GR.

553 In dose response experiments, SVI and GR of each concentration at each timepoint for each
554 drug is calculated, then fitted into a sigmoidal curve:

555 $\mathrm{SVI}\,(\mathrm{c}) = \mathrm{SVI}_{\mathrm{min}} + \frac{100-SVI_{min}}{100+(\frac{c}{SVI50})^{hSVI}}$ $\mathrm{GR}\,(\mathrm{c}) = \mathrm{GR}_{\mathrm{min}} + \frac{1-GR_{min}}{1+(\frac{c}{GRE50})^{hGR}}$

556 The fitted parameters are:

557 SVI_{min} or GR_{min}: the maximum possible effect of a drug on parasite viability or growth inhibition
558 in a fitted curve

559 hSVI or hGR: the hill slope coefficient of the fitted curve

560 SVI50 or GRE50: the concentration that confers half maximal effect on parasite viability or half
561 maximal effect in GR curve.

562 **Imaging and quantification, and transmitted light imaging for deep learning**

563 For fixed timepoints, plates were fixed and stained with 5µg/ml Hoechst and 1% glutaraldehyde.
564 Imaging was performed using Lionheart FX (Biotek) or ImageXpress (Molecular device). Whole
565 wells were captured for all 384 wells with 4X magnification. DAPI intensity and focus was
566 determined using untreated wells as reference High content analysis was performed using
567 image metrics including colony number, size, area, and signal intensity. We found a minimum
568 size of 20 µm of colonies to allows for most optimal removal of small backgrounds and small
569 artefacts. The number of colonies and the area of each colony were then exported for further
570 analysis. Identified outliers were verified on the corresponding images and then discarded.

571 NF54-GFP parasite was used for the generation of deep learning training datasets. Whole well
572 transmitted light images were acquired with 4X magnification using ImageXpress. The same
573 sample was first imaged through transmitted light microcopy then immediately followed by GFP
574 channel to acquire GFP reference image. In a continuous experiment, the plate was returned to
575 culture condition and imaged again at next timepoint.

576 **Image processing and training data preparation**

577 Original TIFF image with resolution of 2048×2048 and depth of 16-bit grayscale was first
578 normalized to 2048×2048 resolution and 8-bit RGB format. The edge of every image was
579 cropped by 150 pixels to remove areas with uneven illumination. All polygon annotations were

initially performed by human professionals. Quality checks of all images and masks were performed with at least two rounds of random selections by two independent reviewers. To optimize computational efficiency and maintain consistent input dimensions across the dataset, all images and masks were downsampled to 512×512 pixels using the Lanczos resampling algorithm[32]. To enable rapid data loading during the iterative training process, all standardized images and their corresponding segmentation masks were subsequently converted to NumPy array format. The dataset was randomly partitioned into training (70%), validation (15%), and test (15%) sets.

Deep Learning U-Net CNN model training

For semantic segmentation, we implemented a U-Net architecture comprising an encoder–decoder structure[33]. The encoder comprises four downsampling stages with 2×2 max pooling, progressively increasing the number of feature channels from 64 to 128, 256, and finally 512. Each stage uses two 3×3 convolutional layers with batch normalization and ReLU activation to capture contextual and morphological features[34-36]. At the bottleneck, feature maps are processed by a double convolution block with 1024 channels to capture high-level semantic features. The decoder mirrors the encoder with four upsampling stages using 2×2 transposed convolutions. Skip connections concatenate encoder features with decoder outputs to preserve spatial details, followed by double convolution blocks for refinement. A final 1×1 convolution produces the single-channel segmentation map for binary classification.

The model was trained using the Adam optimizer with an initial learning rate of 1×10^{-4} and an adaptive scheduler that reduced the rate after 5 stagnant validation epochs[37]. Training was conducted over 50 epoch with a batch size of 32, and validation performance was monitored to prevent overfitting. The final model was selected based on the best validation score, with all metrics reported on a held-out test set. Visual explanations of the model is generated using Grad-CAM to derive attention heatmaps across model layers[38].

605 **Colony quantification**

606 Following segmentation, automated quantification of colony number and area was performed on
607 the predicted binary masks, where white regions (pixel value = 1) represent identified colonies
608 and black regions (pixel value = 0) represent background. Colony enumeration was achieved
609 through connected component labeling. We employed 8-connectivity (Moore neighborhood) for
610 the connected component analysis, which considers pixels connected through both edges and
611 corners as belonging to the same colony. The algorithm iteratively groups adjacent positive
612 pixels until all connected regions are identified, with the total number of distinct labels
613 corresponding to the colony count. Colony areas were quantified by calculating the sum of
614 positive pixels within each segmented region. The total colonization density for each image was
615 computed as the aggregate sum of all positive pixels in the binary mask.

616 **Performance evaluation and metrics**

617 To evaluate colony enumeration, we used Mean Absolute Error (MAE), Root Mean Squared
618 Error (RMSE), Exact Match Rate, tolerance-based accuracy (±1 and ±2 colonies), and the
619 Pearson correlation coefficient to assess counting precision and consistency. For colony
620 segmentation, we evaluated performance using standard pixel-wise metrics, including
621 Intersection over Union (IoU), pixel accuracy, precision, recall, and F1 score, computed from
622 binary masks of predicted and ground truth annotations.

623 **Vision transformer model for semantic segmentation**

624 As an alternative approach to the U-Net architecture, we implemented a Vision Transformer
625 (ViT) model adapted for semantic segmentation[39]. All 512×512 input images were divided into
626 non-overlapping patches of 16×16 pixels, resulting in a sequence of 1024 patches (32×32 grid).
627 To preserve spatial information, learnable position embeddings are added to the patch

embeddings, which were then processed through a stack of transformer encoder layers, with layer normalization and residual connections.

For adapting the transformer to dense prediction, the sequence of output embeddings from the final transformer layer must be reshaped back to a 2D spatial representation and upsampled to match the original image resolution. This is achieved through a decoder head that first reshapes the patch tokens back to their spatial configuration, then applies successive upsampling layers to recover the full 512×512 resolution, ultimately producing pixel-wise binary predictions for colony segmentation. We followed the same training strategy and image processing settings for ViT model as well.

Acknowledgements

We greatly appreciate Dr. David Fidock for the Dd2 K13 mutant lines and NF54 GFP line. We Gratefully acknowledge NIH (R21 AI168803) and Georgia Research Alliance for funding support. We thank Medicines for Malaria Venture for the reference anti-malarial compound library.

1. Witkowski B, Amaratunga C, Khim N, Sreng S, Chim P, Kim S, Lim P, Mao S, Sopha C, Sam B, Anderson JM, Duong S, Chuor CM, Taylor WR, Suon S, Mercereau-Puijalon O, Fairhurst RM, Menard D. Novel phenotypic assays for the detection of artemisinin-resistant Plasmodium falciparum malaria in Cambodia: in-vitro and ex-vivo drug-response studies. Lancet Infect Dis. 2013;13(12):1043-9. Epub 20130911. doi: 10.1016/s1473-3099(13)70252-4. PubMed PMID: 24035558; PMCID: PMC5015432.
2. Davis SZ, Singh PP, Vendrely KM, Shoue DA, Checkley LA, McDew-White M, Button-Simons KA, Cassady Z, Sievert MAC, Foster GJ, Nosten FH, Anderson TJC, Ferdig MT. The extended recovery ring-stage survival assay provides a superior association with patient clearance half-life and increases throughput. Malaria Journal. 2020;19(1):54. doi: 10.1186/s12936-020-3139-6.
3. Baniecki ML, Wirth DF, Clardy J. High-Throughput Plasmodium falciparum Growth Assay for Malaria Drug Discovery. Antimicrobial Agents and Chemotherapy. 2007;51(2):716-23. doi: doi:10.1128/aac.01144-06.
4. Quashie NB, Duah NO, Abuaku B, Quaye L, Ayanful-Torgby R, Akwoviah GA, Kweku M, Johnson JD, Lucchi NW, Udhayakumar V, Duplessis C, Kronmann KC, Koram KA. A SYBR Green 1-based in vitro test of susceptibility of Ghanaian Plasmodium falciparum clinical isolates to a panel of anti-malarial drugs. Malaria Journal. 2013;12(1):450. doi: 10.1186/1475-2875-12-450.
5. Amaratunga C, Neal AT, Fairhurst RM. Flow cytometry-based analysis of artemisinin-resistant Plasmodium falciparum in the ring-stage survival assay. Antimicrob Agents Chemother. 2014;58(8):4938-40. Epub 20140527. doi: 10.1128/aac.02902-14. PubMed PMID: 24867976; PMCID: PMC4136004.
6. Barrett MP, Kyle DE, Sibley LD, Radke JB, Tarleton RL. Protozoan persister-like cells and drug treatment failure. Nature Reviews Microbiology. 2019;17(10):607-20. doi: 10.1038/s41579-019-0238-x.
7. Pandit K, Surolia N, Bhattacharjee S, Karmodiya K. The many paths to artemisinin resistance in Plasmodium falciparum. Trends Parasitol. 2023;39(12):1060-73. Epub 20231011. doi: 10.1016/j.pt.2023.09.011. PubMed PMID: 37833166.
8. Codd A, Teuscher F, Kyle DE, Cheng Q, Gatton ML. Artemisinin-induced parasite dormancy: a plausible mechanism for treatment failure. Malaria Journal. 2011;10(1):56. doi: 10.1186/1475-2875-10-56.
9. Tucker MS, Mutka T, Sparks K, Patel J, Kyle DE. Phenotypic and genotypic analysis of in vitro-selected artemisinin-resistant progeny of Plasmodium falciparum. Antimicrob Agents Chemother. 2012;56(1):302-14. Epub 20111114. doi: 10.1128/aac.05540-11. PubMed PMID: 22083467; PMCID: PMC3256069.
10. Hott A, Tucker MS, Casandra D, Sparks K, Kyle DE. Fitness of artemisinin-resistant Plasmodium falciparum in vitro. J Antimicrob Chemother. 2015;70(10):2787-96. Epub 20150722. doi: 10.1093/jac/dkv199. PubMed PMID: 26203183; PMCID: PMC4668880.
11. Witkowski B, Lelièvre J, Barragán MJ, Laurent V, Su XZ, Berry A, Benoit-Vical F. Increased tolerance to artemisinin in Plasmodium falciparum is mediated by a quiescence mechanism. Antimicrob Agents Chemother. 2010;54(5):1872-7. Epub 20100216. doi: 10.1128/aac.01636-09. PubMed PMID: 20160056; PMCID: PMC2863624.

12. Tripathi J, Stoklasa M, Nayak S, En Low K, Qian Hui Lee E, Duong Tien QH, Rénia L, Malleret B, Bozdech Z. The artemisinin-induced dormant stages of Plasmodium falciparum exhibit hallmarks of cellular quiescence/senescence and drug resilience. Nature Communications. 2024;15(1):7485. doi: 10.1038/s41467-024-51846-0.
13. White NJ, Watson J, Ashley EA. Split dosing of artemisinins does not improve antimalarial therapeutic efficacy. Sci Rep. 2017;7(1):12132. Epub 20170921. doi: 10.1038/s41598-017-12483-4. PubMed PMID: 28935919; PMCID: PMC5608907.
14. Teuscher F, Gatton ML, Chen N, Peters J, Kyle DE, Cheng Q. Artemisinin-induced dormancy in plasmodium falciparum: duration, recovery rates, and implications in treatment failure. J Infect Dis. 2010;202(9):1362-8. doi: 10.1086/656476. PubMed PMID: 20863228; PMCID: PMC2949454.
15. Gnädig NF, Stokes BH, Edwards RL, Kalantarov GF, Heimsch KC, Kuderjavy M, Crane A, Lee MCS, Straimer J, Becker K, Trakht IN, Odom John AR, Mok S, Fidock DA. Insights into the intracellular localization, protein associations and artemisinin resistance properties of Plasmodium falciparum K13. PLOS Pathogens. 2020;16(4):e1008482. doi: 10.1371/journal.ppat.1008482.
16. Thomas JA, Collins CR, Das S, Hackett F, Graindorge A, Bell D, Deu E, Blackman MJ. Development and Application of a Simple Plaque Assay for the Human Malaria Parasite Plasmodium falciparum. PLoS One. 2016;11(6):e0157873. Epub 20160622. doi: 10.1371/journal.pone.0157873. PubMed PMID: 27332706; PMCID: PMC4917082.
17. Hafner M, Niepel M, Chung M, Sorger PK. Growth rate inhibition metrics correct for confounders in measuring sensitivity to cancer drugs. Nature Methods. 2016;13(6):521-7. doi: 10.1038/nmeth.3853.
18. Ariey F, Witkowski B, Amaratunga C, Beghain J, Langlois AC, Khim N, Kim S, Duru V, Bouchier C, Ma L, Lim P, Leang R, Duong S, Sreng S, Suon S, Chuor CM, Bout DM, Ménard S, Rogers WO, Genton B, Fandeur T, Miotto O, Ringwald P, Le Bras J, Berry A, Barale JC, Fairhurst RM, Benoit-Vical F, Mercereau-Puijalon O, Ménard D. A molecular marker of artemisinin-resistant Plasmodium falciparum malaria. Nature. 2014;505(7481):50-5. Epub 20131218. doi: 10.1038/nature12876. PubMed PMID: 24352242; PMCID: PMC5007947.
19. Straimer J, Gnädig NF, Witkowski B, Amaratunga C, Duru V, Ramadani AP, Dacheux M, Khim N, Zhang L, Lam S, Gregory PD, Urnov FD, Mercereau-Puijalon O, Benoit-Vical F, Fairhurst RM, Ménard D, Fidock DA. K13-propeller mutations confer artemisinin resistance in Plasmodium falciparum clinical isolates. Science. 2015;347(6220):428-31. doi: doi:10.1126/science.1260867.
20. Stewart LB, Escolar EL, Philpott J, Cox-Singh J, Singh B, Conway DJ. Intrinsic multiplication rate variation of Plasmodium falciparum in clinical isolates prior to elimination in Malaysia. International Journal for Parasitology. 2025. doi: https://doi.org/10.1016/j.ijpara.2025.02.003.
21. Behrens Hannah M, Schmidt S, Henshall Isabelle G, López-Barona P, Peigney D, Sabitzki R, May J, Maïga-Ascofaré O, Spielmann T. Impact of different mutations on Kelch13 protein levels, ART resistance, and fitness cost in Plasmodium falciparum parasites. mBio. 2024;15(6):e01981-23. doi: 10.1128/mbio.01981-23.
22. Association of mutations in the Plasmodium falciparum Kelch13 gene (Pf3D7_1343700) with parasite clearance rates after artemisinin-based treatments-a

WWARN individual patient data meta-analysis. BMC Med. 2019;17(1):1. Epub 20190117. doi: 10.1186/s12916-018-1207-3. PubMed PMID: 30651111; PMCID: PMC6335805.
23. Looareesuwan S, Kyle DE, Viravan C, Vanijanonta S, Wilairatana P, Charoenlarp P, Canfield CJ, Webster HK. Treatment of patients with recrudescent falciparum malaria with a sequential combination of artesunate and mefloquine. Am J Trop Med Hyg. 1992;47(6):794-9. doi: 10.4269/ajtmh.1992.47.794. PubMed PMID: 1471736.
24. Hott A, Casandra D, Sparks KN, Morton LC, Castanares GG, Rutter A, Kyle DE. Artemisinin-resistant Plasmodium falciparum parasites exhibit altered patterns of development in infected erythrocytes. Antimicrob Agents Chemother. 2015;59(6):3156-67. Epub 20150316. doi: 10.1128/aac.00197-15. PubMed PMID: 25779582; PMCID: PMC4432152.
25. Wang P, Read M, Sims PF, Hyde JE. Sulfadoxine resistance in the human malaria parasite Plasmodium falciparum is determined by mutations in dihydropteroate synthetase and an additional factor associated with folate utilization. Mol Microbiol. 1997;23(5):979-86. doi: 10.1046/j.1365-2958.1997.2821646.x. PubMed PMID: 9076734.
26. Starzengruber P, Fuehrer HP, Swoboda P, Ganesh D, Haque R, Khan WA, Graninger W, Noedl H. Mirincamycin, an old candidate for malaria combination treatment and prophylaxis in the 21st century: in vitro interaction profiles with potential partner drugs in continuous culture and field isolates. Malar J. 2014;13:228. Epub 20140610. doi: 10.1186/1475-2875-13-228. PubMed PMID: 24916383; PMCID: PMC4059879.
27. Yeo AE, Rieckmann KH. Increased antimalarial activity of azithromycin during prolonged exposure of Plasmodium falciparum in vitro. Int J Parasitol. 1995;25(4):531-2. doi: 10.1016/0020-7519(94)00119-9. PubMed PMID: 7635629.
28. Teuscher F, Chen N, Kyle DE, Gatton ML, Cheng Q. Phenotypic changes in artemisinin-resistant Plasmodium falciparum lines in vitro: evidence for decreased sensitivity to dormancy and growth inhibition. Antimicrob Agents Chemother. 2012;56(1):428-31. Epub 20111010. doi: 10.1128/aac.05456-11. PubMed PMID: 21986828; PMCID: PMC3256014.
29. Kümpornsin K, Kochakarn T, Yeo T, Okombo J, Luth MR, Hoshizaki J, Rawat M, Pearson RD, Schindler KA, Mok S, Park H, Uhlemann A-C, Jana GP, Maity BC, Laleu B, Chenu E, Duffy J, Moliner Cubel S, Franco V, Gomez-Lorenzo MG, Gamo FJ, Winzeler EA, Fidock DA, Chookajorn T, Lee MCS. Generation of a mutator parasite to drive resistome discovery in Plasmodium falciparum. Nature Communications. 2023;14(1):3059. doi: 10.1038/s41467-023-38774-1.
30. RIVADENEIRA EM, WASSERMAN M, ESPINAL CT. Separation and Concentration of Schizonts of Plasmodium falciparum by Percoll Gradients. The Journal of Protozoology. 1983;30(2):367-70. doi: https://doi.org/10.1111/j.1550-7408.1983.tb02932.x.
31. Lambros C, Vanderberg JP. Synchronization of Plasmodium falciparum erythrocytic stages in culture. J Parasitol. 1979;65(3):418-20. PubMed PMID: 383936.
32. Duchon CE. Lanczos Filtering in One and Two Dimensions. Journal of Applied Meteorology and Climatology. 1979;18(8):1016-22. doi: https://doi.org/10.1175/1520-0450(1979)018<1016:LFIOAT>2.0.CO;2.

33. Ronneberger O, Fischer, P. & Brox, T. U-net: convolutional networks for biomedical image segmentation. In Proc. 18th International Conference on Medical Image Computing and Computer-Assisted Intervention (eds Navab, N. et al.) 234–241. Springer. 2015.
34. Agarap AF. Deep Learning using Rectified Linear Units (ReLU). Preprint at https://arxivorg/abs/180308375 (2018). 2018.
35. Lecun Y, Bottou L, Bengio Y, Haffner P. Gradient-based learning applied to document recognition. Proceedings of the IEEE. 1998;86(11):2278-324. doi: 10.1109/5.726791.
36. Fukushima K. Visual Feature Extraction by a Multilayered Network of Analog Threshold Elements. IEEE Transactions on Systems Science and Cybernetics. 1969;5(4):322-33. doi: 10.1109/TSSC.1969.300225.
37. Diederik P. Kingma JB. Adam: A Method for Stochastic Optimization. Preprint at https://arxivorg/abs/14126980 (2014). 2014.
38. Ramprasaath R. Selvaraju MC, Abhishek Das, Ramakrishna Vedantam, Devi Parikh, Dhruv Batra. Grad-CAM: Visual Explanations from Deep Networks via Gradient-based Localization. Preprint at https://arxivorg/abs/161002391. 2016.
39. Alexey Dosovitskiy LB, Alexander Kolesnikov, Dirk Weissenborn, Xiaohua Zhai, Thomas Unterthiner, Mostafa Dehghani, Matthias Minderer, Georg Heigold, Sylvain Gelly, Jakob Uszkoreit, Neil Houlsby. An Image is Worth 16x16 Words: Transformers for Image Recognition at Scale. Preprint at https://arxivorg/abs/201011929. 2020.

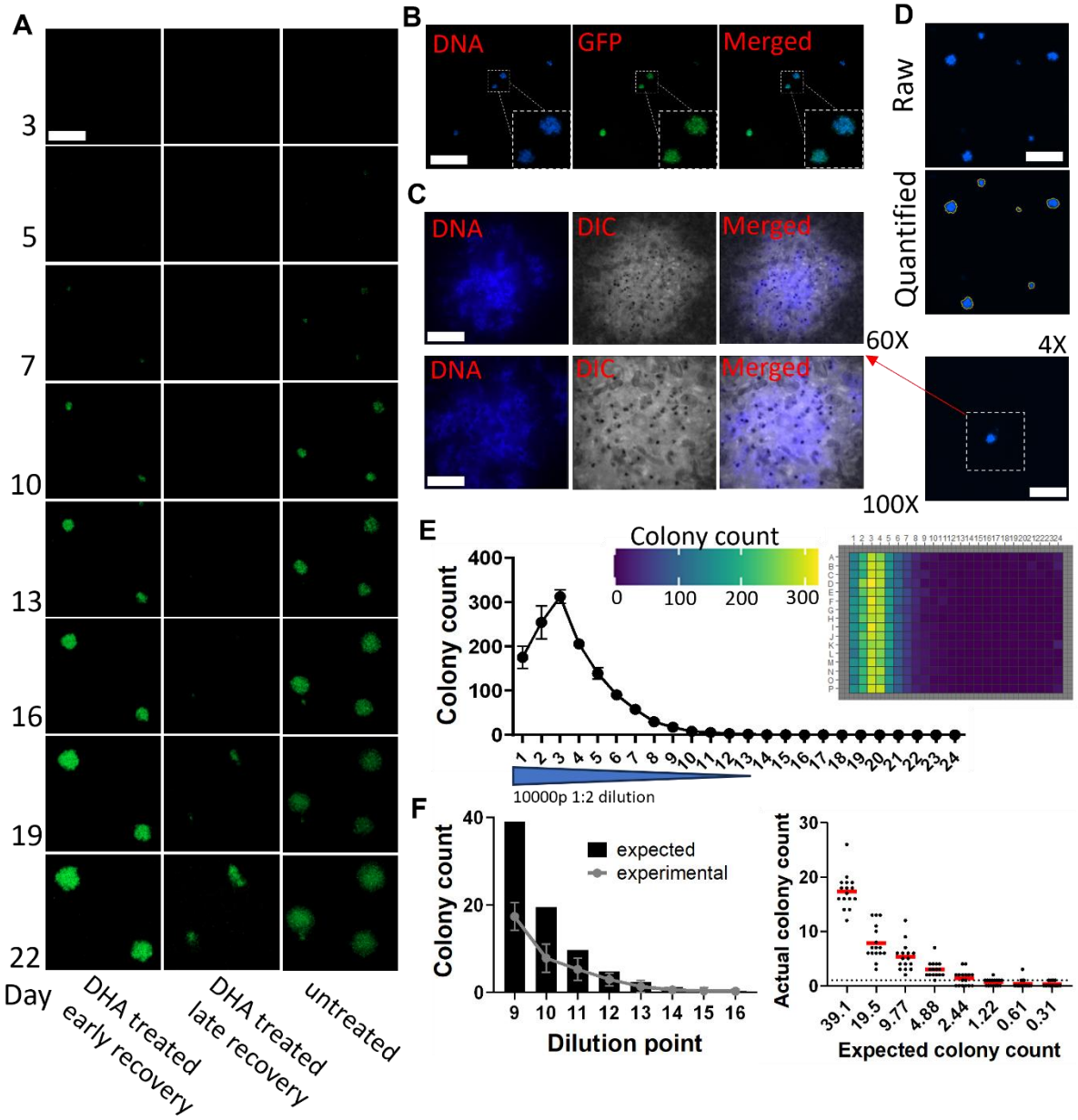

809

810

811

812

813

814

815 **Fig. 1. A single parasite grows into a colony. (A)** Growth of the same individual NF54-GFP
816 colonies imaged over time, with or without 6h DHA exposure (Scale bar = 150μm). **(B)** Hoechst
817 stained and GFP fluorescent images of day 7 parasite colonies imaged with a 4X objective;
818 white boxes show the same colonies imaged with a 20X objective (Scale bar = 100μm) **(C)**
819 Higher magnification images of a day 7 parasite colony. The observed black dots are hemozoin.
820 Top: imaged with a 60X objective (scale bar = 25μm), bottom: imaged with a 100X objective
821 (scale bar =15μm). The 4X objective image scale bar = 100μm. **(D)** High-content image analysis
822 was used to measure the number and the size of colonies of a fraction of a well (Full well is
823 shown in Fig. S1C) (Scale bar = 100μm). **(E)** Average number of colonies in each column of
824 each dilution point (left) and heatmap view of colony counts of the same serial dilution plate
825 (right). Dilution points 1 and 2 could not be accurately quantified due to wells having too many
826 colonies. **(F)** Comparison between experimental results and estimated numbers in low dilution
827 points (left) and comparison of the number of colonies between quantified and expected number
828 of positive wells (right). The estimated colony numbers are shown in Fig. S3A. All experiments
829 were performed at least twice.

830

831

832

833

834

835

836

837

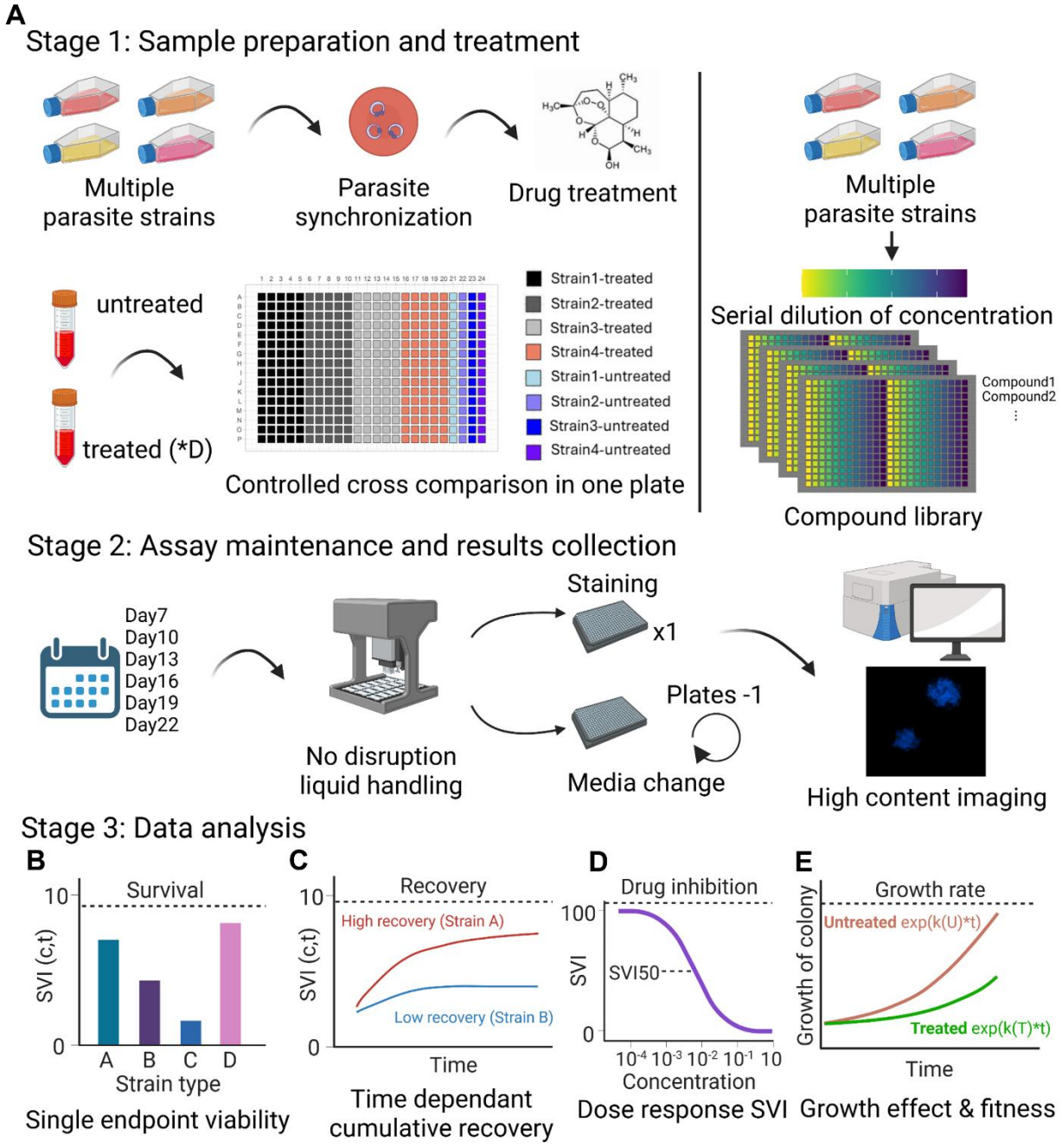
A
Stage 1: Sample preparation and treatment
Multiple parasite strains
Parasite synchronization
Drug treatment
untreated
treated (*D)
Strain1-treated
Strain2-treated
Strain3-treated
Strain4-treated
Strain1-untreated
Strain2-untreated
Strain3-untreated
Strain4-untreated
Controlled cross comparison in one plate
Multiple parasite strains
Serial dilution of concentration
Compound1
Compound2
Compound library
Stage 2: Assay maintenance and results collection
Day7
Day10
Day13
Day16
Day19
Day22
No disruption liquid handling
Staining
x1
Plates -1
Media change
High content imaging
Stage 3: Data analysis
B
Survival
SVI (c,t)
Strain type
Single endpoint viability
C
Recovery
High recovery (Strain A)
Low recovery (Strain B)
Time
Time dependant cumulative recovery
D
Drug inhibition
SVI
SVI50
Concentration
Dose response SVI
E
Growth rate
Growth of colony
Untreated exp(k(U)*t)
Treated exp(k(T)*t)
Time
Growth effect & fitness

843 **Fig. 2. qTRACE simultaneously reports viability, time-dependent recovery, and growth**
844 **effects at single parasite resolution. (A)** Schematics of the qTRACE process. In stage 1,
845 parasite strains are prepared and treated with drugs. Treated and untreated samples are
846 prepared based on the dilution factor D, then plated on the same plate. Left side showing
847 representative DHA exposure workflow and right side showing representative drug testing
848 workflow. In stage 2, plates undergo automated media change, and one plate is taken for HCI at
849 each designated timepoint. In Stage 3, data are analyzed as described in Fig. 2B-E. **(B)** Single
850 endpoint SVI assessments to evaluate percentage viability at concentration c and time t. **(C)**
851 Assessments of SVI at multiple time points to evaluate time-dependent recovery or drug effects.
852 **(D)** SVI assessments in a dose response. SVI50 is the concentration of a drug that estimates
853 50% of parasites were viable. **(E)** Assessments of exponential growth of colonies under different
854 conditions or between different strains to evaluate growth effects and fitness. Growth Rate (GR)
855 is then derived using variable K between two conditions.

856

857

858

859

860

861

862

863

864

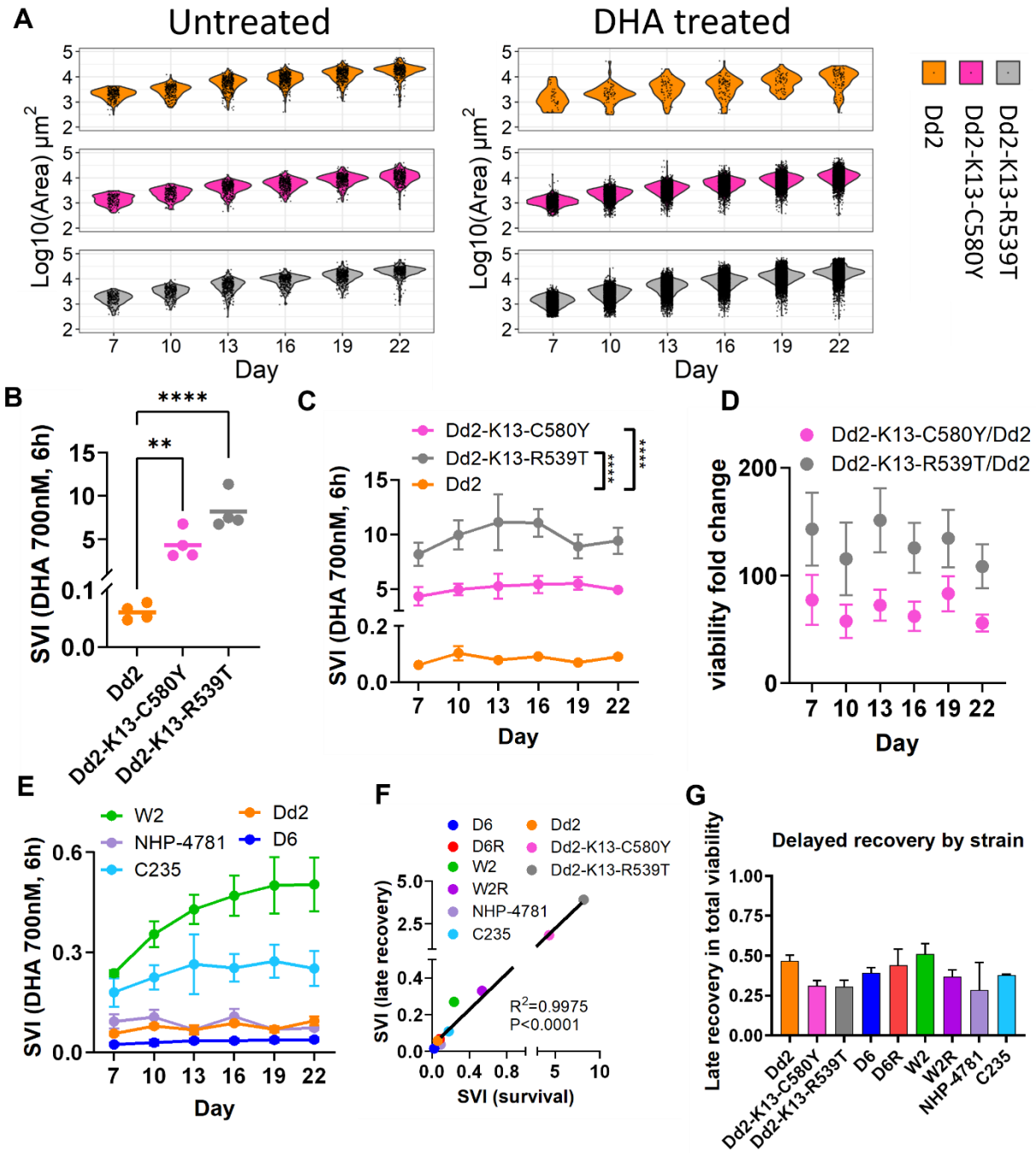

865

866

867

868

869 **Fig. 3. qTRACE reveals differential susceptibility and recovery from DHA exposure**
870 **across various parasite lines. (A)** Individual colonies and the sizes of each colony under
871 untreated condition (left) and DHA condition (right) for every timepoint recorded from Dd2 and
872 Dd2 K13 mutants. Each black dot represents one colony. From two biological replicates. **(B)** SVI
873 assessment of Dd2 and Dd2 K13 mutants on day 7 quantifying initial survival from DHA
874 exposure, n=80 technical replicates and n=4 biological replicates. P-value calculated from one-
875 way Anova. **(C)** Time-dependent SVI of Dd2 and Dd2 K13 mutants at continuous timepoints,
876 day 19 and 22 for Dd2-K13-R539T were not accurately quantified due to colony overgrowth.
877 n=80 technical replicates and n=4 biological replicates. P-value calculated from two-way Anova.
878 **(D)** The fold change in SVI between Dd2 and Dd2-K13-C580Y, as well as between Dd2 and
879 Dd2-K13-R539T, for all timepoints. **(E)** Time dependent recovery SVI of five artemisinin
880 sensitive strains at continuous timepoints. n=80 technical replicates and n=3 biological
881 replicates. **(F)** Comparison of late recovery SVI (Max SVI-survival SVI) and survival SVI of all
882 nine parasite lines with linear regression. P-value and R^2 value calculated using Pearson's
883 correlation. **(G)** Proportion of late recovery in total viability over entire 22 days across nine
884 parasite lines (error bar=SEM). Additional data in Supplementary Table 1.

885

886

887

888

889

890

891

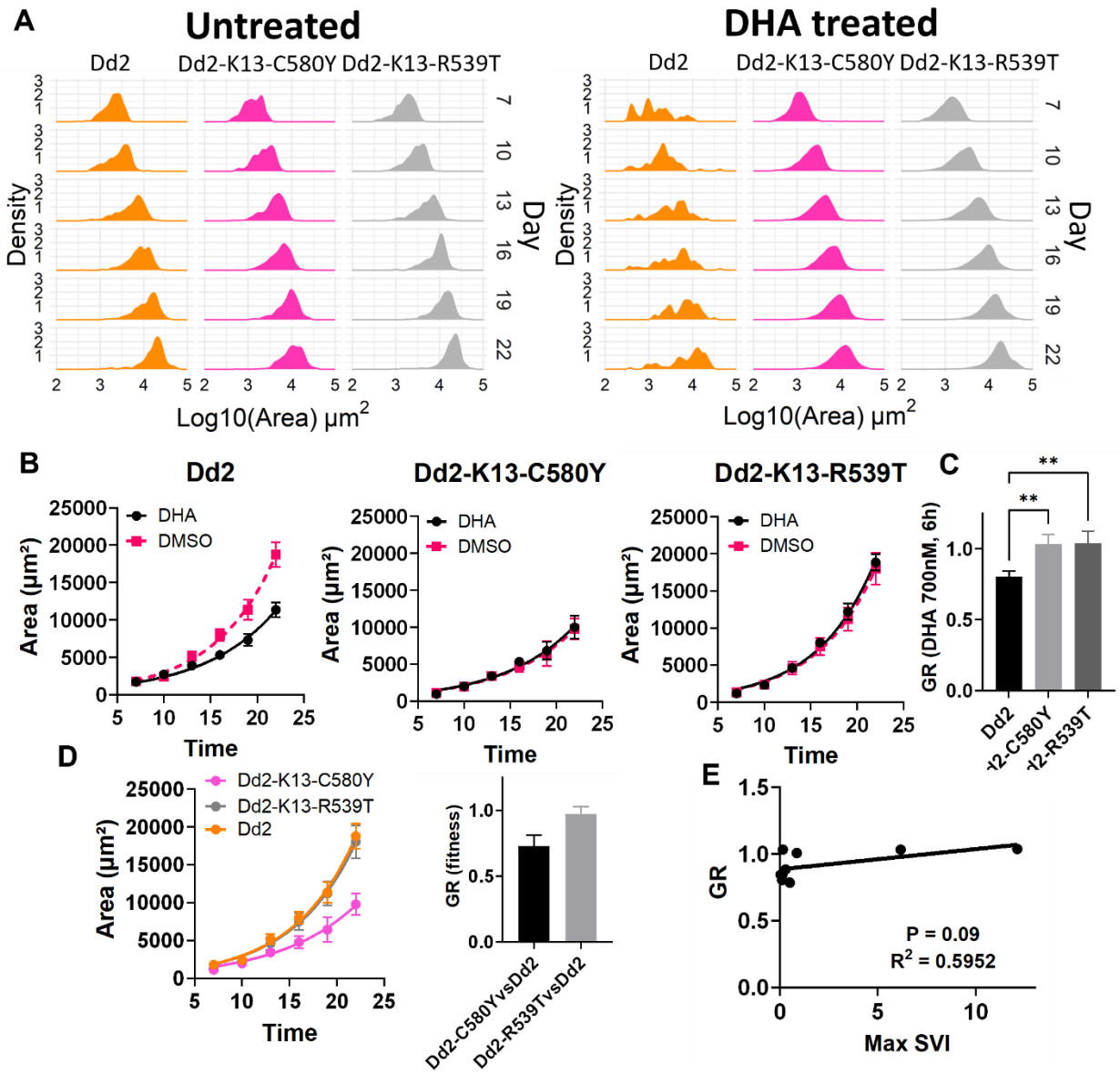

892

893

894

895

896

897

898

899 **Fig. 4. Growth impacts induced by DHA and fitness costs to artemisinin resistance. (A)**
900 Density distribution of colony sizes in Dd2 and Dd2 K13 mutants at continuous timepoints in
901 DHA and DMSO conditions. From two biological replicates. **(B)** Fitted growth curves of
902 averaged colony sizes at all timepoints for Dd2 (left), Dd2-K13-C580Y (middle), and Dd2-K13-
903 R539T (right) in DHA condition and DMSO condition. n=80 technical replicates and n=4
904 biological replicates. **(C)** GR values of Dd2 and Dd2 K13 mutants comparing DHA condition to
905 DMSO condition for each strain. P-value calculated from one-way Anova. **(D)** Fitted growth
906 curves of averaged colony sizes at all timepoints for Dd2 and Dd2 K13 mutants without any
907 treatment (left) and GR values between parasite lines (right). n=80 technical replicates and n=4
908 biological replicates. **(E)** Correlation comparison between Max SVI and GR for all nine parasite
909 lines tested with linear regression. P-value and R^2 value calculated using Pearson's correlation.
910 Additional data in Supplementary Table 2.

911

912

913

914

915

916

917

918

919

920

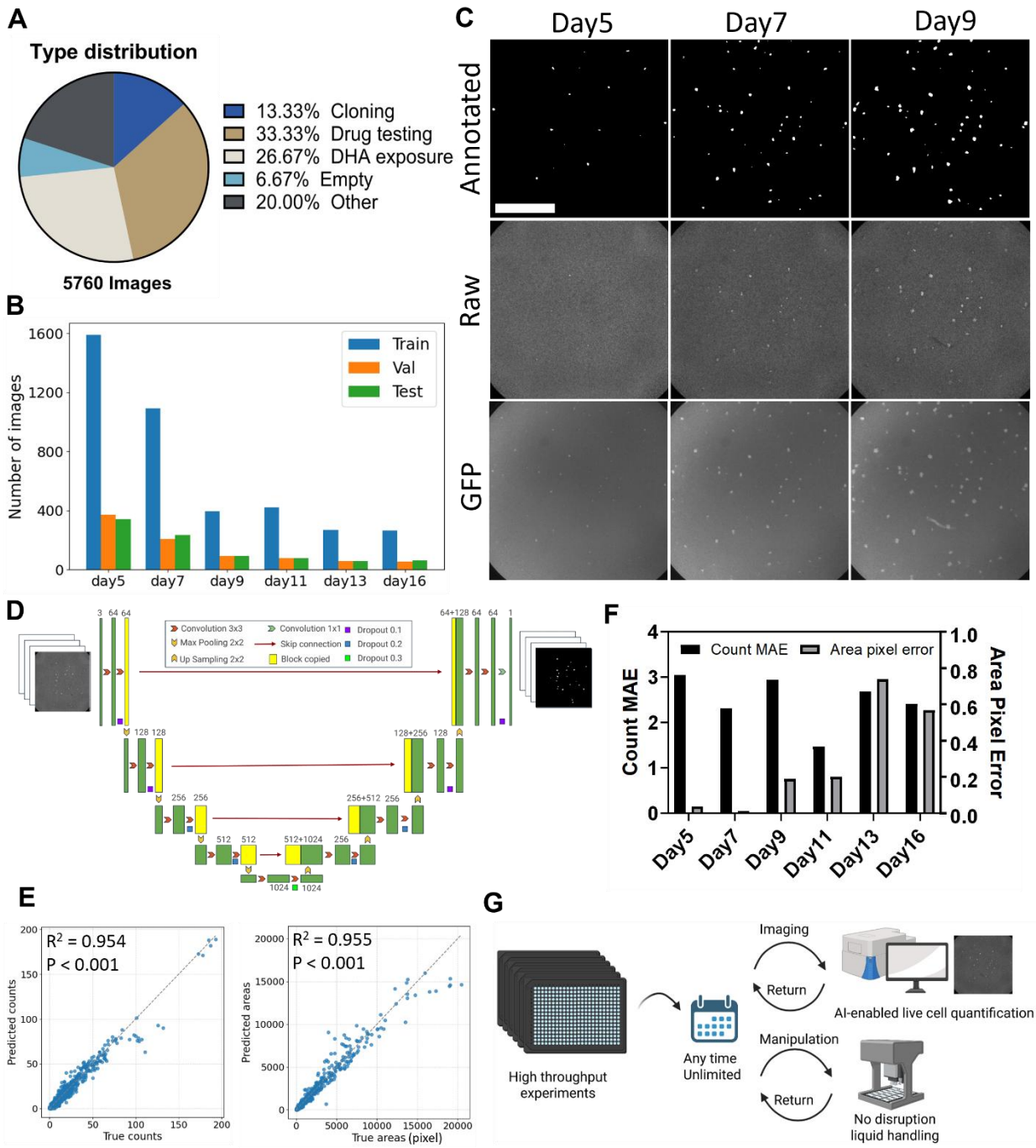

921

922

923

924

925 **Fig. 5. Deep learning enables continuous label-free live cell analysis. (A)** Distribution of
926 training datasets by types of experiments. **(B)** Distribution of training datasets by time points and
927 training, validation, and test. **(C)** Representative raw transmitted light images and human
928 annotated mask images for a continuous experiment. GFP was used as annotation reference to
929 confirm authenticity of colonies on transmitted light images. Scale bar 1000μm. **(D)** Schematics
930 of model architecture and qTRACE AI application. The architecture consists of a contracting
931 path (left side) and an expanding path (right side) with skip connections (red arrows) that
932 concatenate feature maps between corresponding layers. Numbers indicate the spatial
933 dimensions and number of feature channels at each layer. **(E)** Evaluation of model prediction
934 accuracy compared to human annotated results for count (left) and area (right). P-value and R^2
935 value calculated using Pearson's correlation. **(F)** Count mean absolute error (MAE) and area
936 pixel error percentage of the trained model by timepoint. **(G)** Schematics showing qTRACE AI
937 workflow. Flexible continuous imaging and manipulation of the same sample over time.

938

939

940

941

942

943

944

945

946

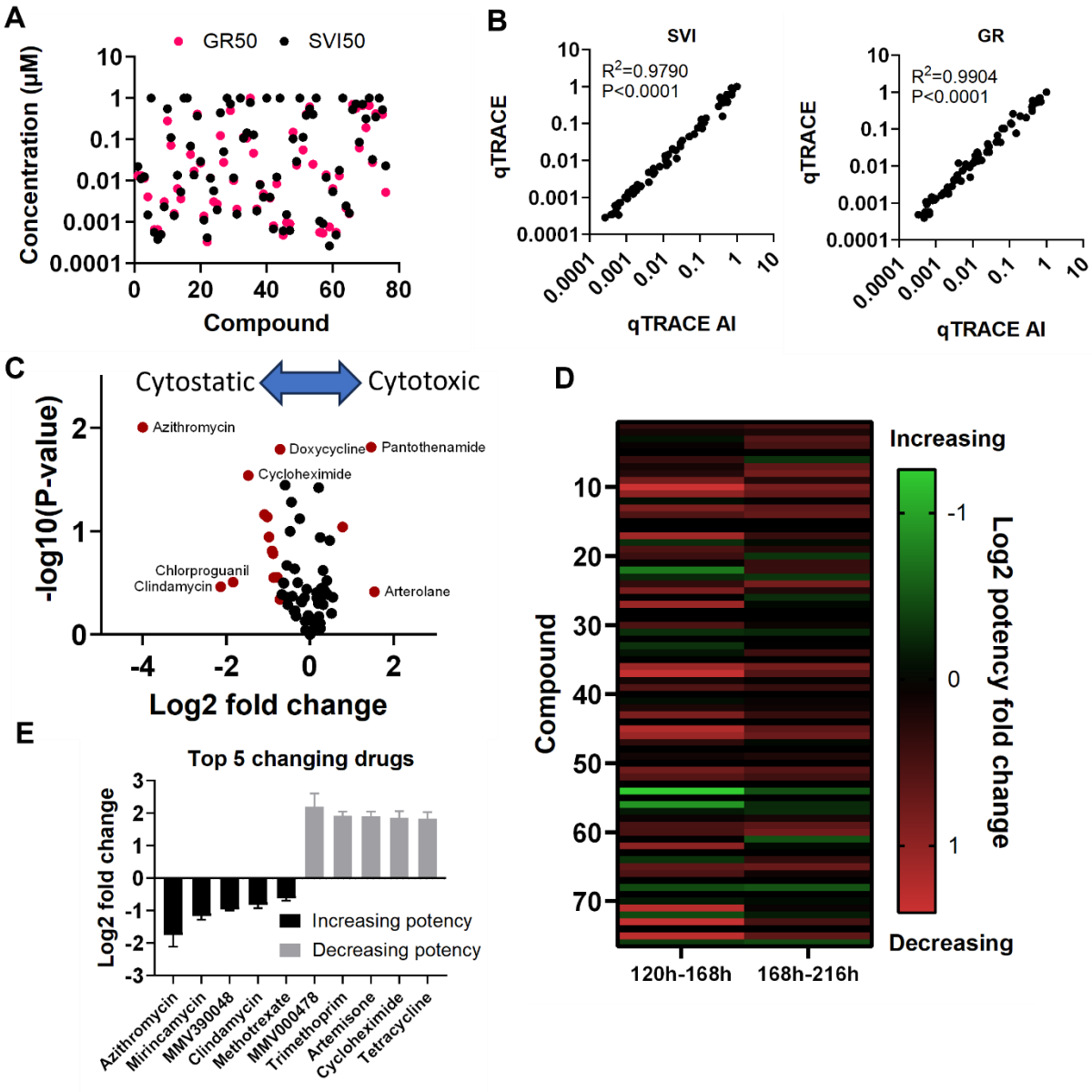

947

948

949

950

951

952

953 **Fig. 6. qTRACE reveals new insights into drug activities and effects. (A)** SVI50 and GR50
954 for drugs tested from MMV antimalarial reference library. n=2 biological replicates. **(B)**
955 Comparison of screening results between qTRACE AI and qTRACE for SVI (left) and GR (right).
956 P-value and R^2 value calculated using Pearson's correlation. **(C)** Cytotoxic and cytostatic effect
957 evaluation of drugs from MMV antimalarial reference library. Shifting in directions represents
958 preference of either cytostatic effect (left) or cytotoxic effect (right). **(D)** Effect of altering time on
959 SVI50 shift for drugs from MMV antimalarial reference library at 48h interval. n=2 biological
960 replicates. **(E)** The five drugs showing the highest potency shift, for each direction, over entire
961 measured time course are shown. Error bar = SEM.

962